



# Automatic detection of Solar Active Regions observed at submillimeter frequencies

A.L.G. Pereira<sup>a1</sup>, C.G. Giménez de Castro<sup>a,b</sup>, J.F.Valle Silva<sup>a</sup>

<sup>a</sup> Centro de Rádio Astronomia e Astrofísica do Mackenzie (CRAAM), Universidade Presbiteriana Mackenzie, São Paulo, Brazil

<sup>b</sup> Instituto de Astronomía y Física del Espacio (IAFE), Buenos Aires, Argentina

Received on Feb, 2018 / Accepted on Jun, 2019

## Abstract

The Solar Submillimeter Telescope (SST) observes simultaneously and independently with a multibeam focal array at 212 and 405 GHz. Since 1999, the SST daily monitors the solar activity generating binary files from which solar maps can be extracted. The identification of Active Regions (AR) in these maps is affected by the strong atmospheric attenuation and inaccuracies of the telescope pointing, therefore, maps are visually inspected to manually extract the AR. This is a lengthy process if one wants to do statistical analysis over the 20 years data set already recorded. To automate the process, we propose artificial intelligence techniques of machine learning and computer vision. A Convolutional Neural Network was created within the Keras framework for the classification of the SST maps and then, a computer vision algorithm in the OpenCV framework for the automatic detection of AR. This hybrid approach allowed the identification of more than 400 active regions between January 2002 and December 2017 and the statistical analysis of their physical properties. Our results were validated by comparing with previous works which were carried out with a visual identification and manual extraction procedure, and we found good agreement.

**Keywords:** SST, Submillimeter Solar Maps, Artificial Intelligence, Convolutional Neural Networks, Keras, Computational View, OpenCV.

## 1. Introduction

Solar Active Regions (AR) are areas of enhanced brightness over the solar disk observed at radio frequencies. They are known since the early 1960s and have been associated with sunspots, plages and strong magnetic fields. For a review of their properties see [31]. Observations at submillimeter frequencies provide insights on the atmospheric structure at chromospheric heights, this information is very valuable to make and validate atmospheric models. There are few studies of the AR properties at submillimeter frequencies and only one with a statistical analysis [11], however restricted to a few observing weeks. Since April 2001, the Solar Submillimeter Telescope (SST, [5]) is the only submillimeter patrol telescope with beam sizes similar to AR characteristic sizes, and therefore, with the capability to undertake long duration studies with a spatial

---

<sup>1</sup> E-mail Corresponding Author: [andrelgpereira@gmail.com](mailto:andrelgpereira@gmail.com)

resolution able to separate emission from the quiet sun and the AR itself. A 20 years data analysis requires computing aid to recognize AR and to extract their physical properties. However, the task can be greatly difficult because of the Earth atmospheric contamination and, in the case of the SST, irregularities in the antenna movement.

Several works have been done using the computational support in data analysis and interpretation. In some fields, like Astronomy, they became a fundamental tool because of the huge data volume. Looking for new techniques to work at the submillimeter range, here we propose an innovative computational approach to detect AR in SST maps. We use Convolutional Neural Network and Computer Vision algorithms to identify AR and obtain their number, size, brightness temperature and flux density, covering 15 years of daily observations from the maximum of Solar Cycle 23 and most of the present 24.

This paper is organized as follows: Section II describes the instrument and data reduction. Section III introduces our methodology to automatically detect AR. Section IV describes the results of applying our methodology and comparisons with previous works. Finally, Section V presents our last remarks.

## **2. The Solar Submillimeter Telescope**

The SST [5] is a multi-beam radio telescope installed at 2,550 m above sea level in the El Leoncito Astronomical Complex (CASLEO for the Spanish acronym) in the Argentinean Andes. It operates simultaneously and independently with six radiometers containing two focal arrays: the main array consists of four beams, three observing at the frequency of 212 GHz, with 4 arcmin half power beam width, (HPBW) partially overlapping, and one beam at 405 GHz (HPBW=2 arcmin). The second array has two additional concentric beams displaced from the center of the main set, with receivers at 212 GHz and 405 GHz (Figure 1). The main goal of the instrument is to observe transient fast phenomena in the Sun atmosphere, like flares, pointing over a selected AR and tracking its path along the day. However, as a calibration procedure, it makes solar maps at different times during the observation. These maps are the data of our work.

### **2.1 Solar map in the submillimeter wavelength with the SST**

SST makes 3 maps every observing day: the six radiometers record the average intensity in units that are linearly proportional to the input power, or, equivalently in radio astronomy, to the source brightness temperature, and create 4 independent maps at 212 GHz and 2 at 405 GHz. For this work we chose to use 40 ms integrated data. The data files have a maximum duration of one hour, while a map takes approximately 10 minutes to be complete. There are currently ~ 300 GB of SST binary raw data stored in our repositories.

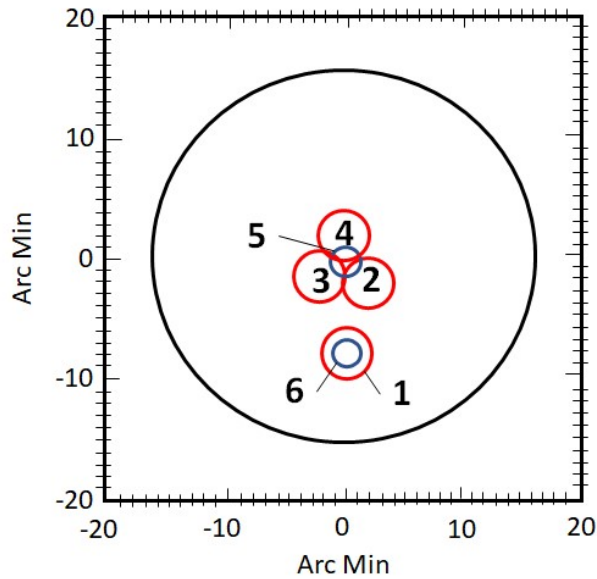


Fig. 1. Projection of SST beams (1 to 6) over the solar disk.

SST solar maps are typically made out of azimuth raster scans (on-the-fly maps) of 90 arcmin length. The elevation changes at every scan to make a square that covers the entire solar disc. Typical separation between scans is 2 arcmin, i.e. half the HPBW at 212 GHz. Scan speed is between 0.1 to 0.2 deg s<sup>-1</sup>; and since we use 40 ms integrated data, these speeds produce a separation in azimuth between successive points between 0.24 arcmin (14.4 arcsec) to 0.48 arcmin (28.8 arcsec), therefore observations are oversampled in azimuth and produce a rectangle “pixel” of (0.24 - 0.48) arcmin x 2 arcmin. The building of a map consists of the following procedure:

1. The binary data are read and maps are identified by a flag called `OPMODE`. When `OPMODE=1, 2, 3, 21, 22` or `23` the antenna is making raster scans to produce a map. In these cases we consider that a map flag is ON.
2. Data are interpolated to produce images with 288 x 288 pixels for 0.11 arcsec pixel<sup>-1</sup> size, and 31 arcmin x 31 arcmin field of view (FOV).
3. A small artificial displacement caused by the antenna movement is eliminated following the procedure described in [17].
4. Alt-Azimuth coordinates are transformed to equatorial.
5. Raw units are transformed to temperature using the quiet Sun brightness temperature as a reference as described in [11].

It is important to notice that every SST receiver produces one independent image, which is different from the others since the receivers point to different places in the sky (see Figure 1). Colors in the images are only used to represent intensities since the receivers work at only one frequency.

Despite this procedure, the identification of solar structures is still hampered, mostly because data are masked by the atmospheric attenuation with optical depths  $\sim 0.3$  and  $1.0$  for 212 and 405 GHz respectively [32]. Moreover, problems with the instrument tracking during the solar scan may also create false structures. Therefore the final image may be useless. In order to prepare an automatic detection system, we visually inspected

samples of data with the map flag ON and found 11 different characteristic images to train our artificial intelligence machine to identify real AR (Figure 2). Image (1) is a map with AR, image (2) is a map **without** AR. Image (3) presents *ghosts* outside the sun disc created by errors in tracking that can mistaken the machine and be discarded although it may contain real AR; (4) is a map with a partial Sun disc due to a wrong command (the center of the map is not the sun center) but it can also contain AR, (5) is elliptical; (6) has disordered raster scans; (7) is too noisy but it is still possible to detect AR; (8) and (9) are pure noise; (10) and (11) have no solar information because problems with the receivers. These 11 characteristic images are needed in order to increase the efficiency of our detection system, without them the number of false positives and false negatives increase making the results unreliable. Moreover, with this classification we reach a 97% level of accuracy against 95% when we use a simple *binary* classification (*good* or *bad*).

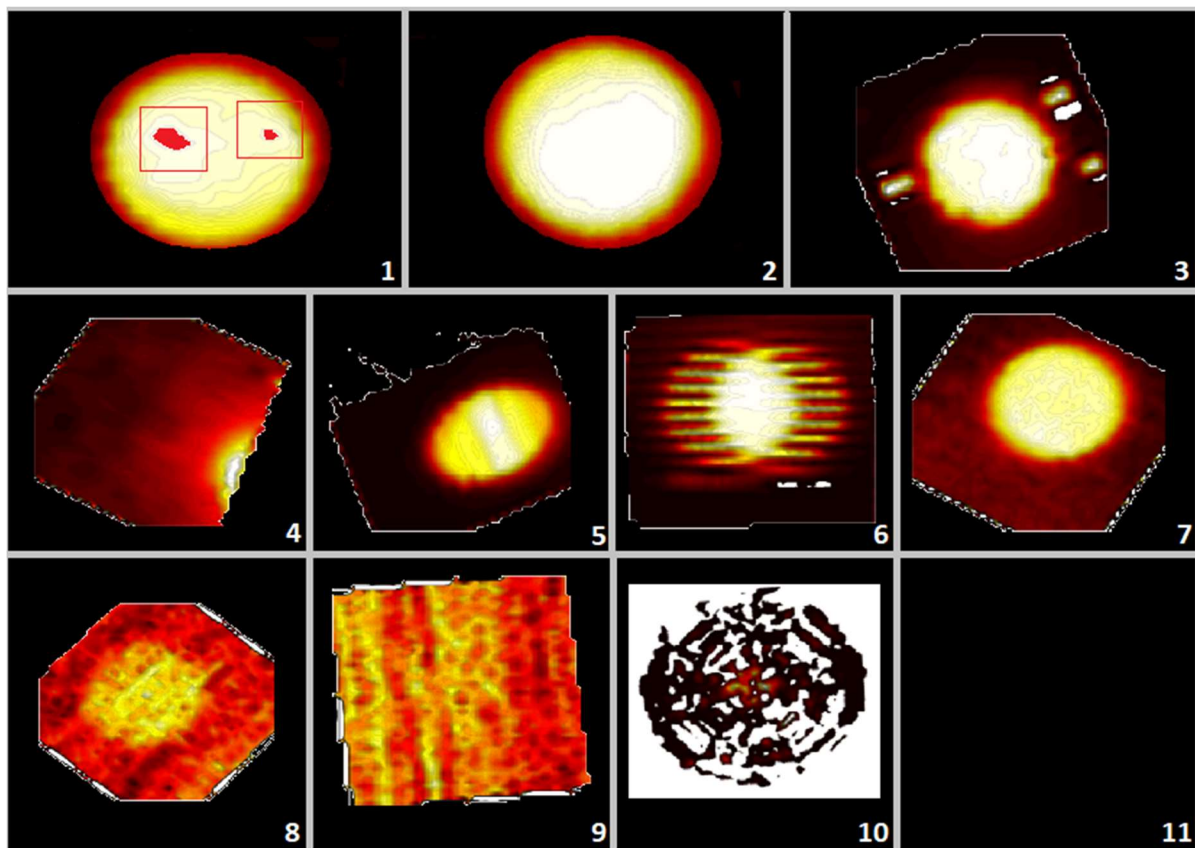


Fig. 2: The eleven characteristic images are shown, see the text for an explanation. The images are in different spatial scales, to show different Field of Views.

We processed data corresponding to the period between January 2002 and December 2017, i.e. from the maximum of the solar cycle 23 until almost the end of cycle 24. We restricted the observation time between 14:00 and 17:00 UT (11:00 to 14:00 local time) when the sun is at its highest elevation and the atmospheric attenuation is lower. We processed, in total, 16,620 maps.

### 3. Methodology

In order to find AR, a hybrid three steps approach was used: (i) the whole image is classified using an Artificial Convolutional Neural Network (ConvNet, [4][18]), within the Keras framework [7] working as a map filter separating only maps with AR; (ii) the

selected maps are then transformed to black and white (binarization) [2] with brighter regions highlighted; and (iii) the AR contour is detected using OpenCV [1][12].

### 3.1 The Convolutional Neural Network Architecture

In the literature there are many artificial convolutional neural network models [14] [15] [16] that can be used for the construction of a model to solve a specific problem. It is known that the quality of a network architecture significantly improves making it deeper and wider. Our motivation, however, was to build a workable ConvNet and demonstrate its usefulness to our research. We started building a very similar LeNet model [14] and introduced changes. We added other two convolutional and pooling layers. For each convolutional layer we set the kernel size (filter) as a 3x3 matrix and for each max pooling layer, we use a window with a size of 2 pixels because smaller filters collect as much local information as possible [24]. So, our final model is described as follows:

- Layer 0 - Input images represented by a 150 x 150 x 3 matrix. (Remember that the color is artificially introduced.)
- Layer 1 - Convolutional Layer: filters the input image with 32 kernel matrices resulting in 32 feature maps of 148 x 148 pixels.
- Layer 2 - Max Pooling: down-samples the previous extracted features to 74 x 74 x 32.
- Layer 3 - Convolutional Layer: filters Layer 2 output with 64 kernel matrices resulting in 64 feature maps of 72 x 72 pixels.
- Layer 4 - Max Pooling: down-samples the previous extracted features to 36 x 36 x 64.
- Layer 5 - Convolutional Layer: filters the Layer 4 output with 64 kernel matrices resulting in 128 feature maps of 34 x 34 pixels.
- Layer 6 - Max Pooling: down-samples the previous extracted features to 17 x 17 x 128.
- Layer 7 - Convolutional Layer: filters the Layer 6 output with 128 kernel matrices resulting in 128 feature maps of 15 x 15 pixels.
- Layer 8 - Max Pooling: down-samples the previous extracted features to 7 x 7 x 128.
- Layer 9 - Flattening (Linearization) of the down sampled Feature Maps from Layer 8 output to a vector with 6,272 elements.
- Layer 10 - Dropout: to weight constraint on those layers at 20% to avoid the data "overfitting".
- Layer 11 - Fully Connected Layer (Dense): with Layer 10 output vector as input that outputs 512 elements.
- Layer 12 - Fully Connected Layer (Dense): that takes Layer 11 output vector and outputs a classification in 11 different image types.

The best hyperparameter values were obtained by manual optimization, see in Table 1 the final and the range of values tested. We chose the Stochastic Gradient Descent (SGD) Optimization Algorithm; but for neuron activation values, was set to Rectified Linear Unit (ReLU) and Sigmoid for the convolutional and dense layers respectively. We used the Keras framework [7] [8], which is freely available, to construct this architecture. The choice of this framework was motivated by its ability to parametrically build neural networks, facilitating a fast construction in a simple and configurable way, encapsulating

several libraries dedicated to the training of deep learning machines such as TensorFlow [9] and Theano [10].

Table 1. Hyperparameters Values adopted for training, and the Range of values tested.

Name	Value	Range
<b>Learning Rate</b>	0.001	0.001; 0.002; 0.01; 0.02; 0.2
<b>Momentum</b>	0.0	0.0; 0.2; 0.4; 0.6; 0.8; 0.9
<b>Batch Size</b>	20	10; 20; 40; 60; 80; 100
<b>Number of Epochs</b>	150	50; 100; 150
<b>Steps by Epoch</b>	100	50; 100; 150
<b>Dropout Rate</b>	0.2	0.0; 0.1; 0.2; 0.3; 0.4; 0.5; 0.6; 0.7; 0.8; 0.9
<b>Kernel weight matrix Inizialization</b>	glorot	Uniform; glorot normal; glorot uniform
<b>Optimization Algorithm</b>	SGD	SGD; RMSprop; Adam

### 3.2 ConvNet Map Classification with Data Augmentation and AR Recognition and Characterization

The ConvNet described above was applied to classify the SST images. Artificial Neural Networks are extremely sensitive to the amount and quality of data used for training and testing [19][22][23]. Data augmentation techniques have been shown to be useful in cases where the sample is insufficient for training and testing. We used algorithms implemented by Keras (ImageDataGenerator Class) for each characteristic Image, and created clones by shifting and rotating the original Images. We increased our sample until we achieved a maximum accuracy of  $\sim 97\%$  for testing and  $\sim 98\%$  for validation generating 5,463 images of each type, i.e. 60,093 samples in total: 60% for training, 20% for validation and 20% for tests. A bigger sample reduced the accuracy, likely because the data augmentation procedures *saturated* and created repeated maps adding some bias to our training samples that doesn't match the original maps. The hardware setup used was composed of a motherboard with an Intel Core i7-6700K (4 cores), 2.6 GHz clock CPU and 32GB of RAM; taking around 10 to 12 hours for training.

To increase the reliability of the AR recognition every training map was compared with images at other wavelengths. The comparison is not an easy task, since there are differences between the images not only in space resolution and sensitivity, but also in the underlying physics. Figure 3 shows an example, where an extreme ultra violet (EUV) image observed at 174 Å with the Atmospheric Imaging Assembly telescope (AIA, [33]) on board the Solar Dynamic Dynamics Observatory (SDO) satellite is compared with radio maps at 212 GHz and 17 GHz from the Nobeyama Radioheliograph (NoRH, [34]). The EUV images come from the high Corona, the submillimeter emission is mostly chromospheric and the millimeter emission is low Corona / high Chromosphere. Moreover the instruments have very different space resolutions (2 arcsec, 4 arcmin and 20 arcsec for EUV, submillimeter and millimeter data respectively). This is why the identification for training purposes was visually man-made. Besides this, since the resolution of the SST beams is of the same size of AR, close features may be characterized

as a single AR (See Figure 3-a and 3-b): the detected AR in the SST map corresponds to two EUV AR.

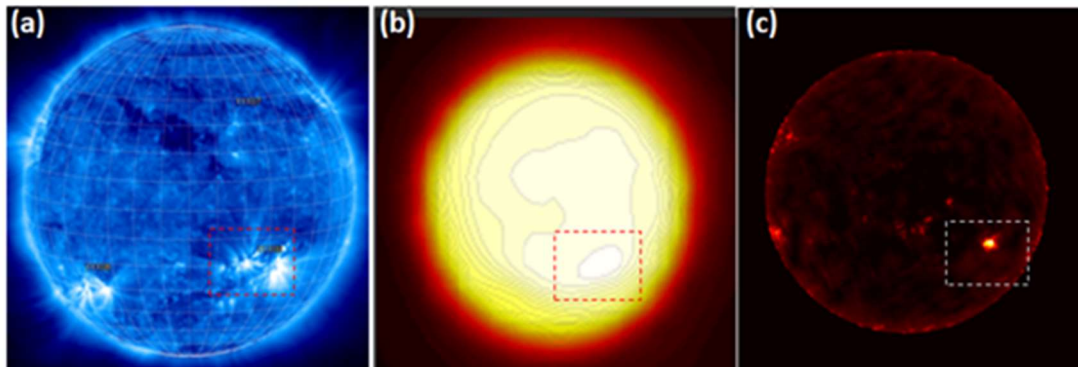


Fig. 3: The same AR observed at different wavelengths and telescopes: (a) AIA image for  $\lambda=174 \text{ \AA}$ ; (b) SST map for  $\lambda=1.4 \text{ mm}$  and (c) NoRH for  $\lambda=17.6 \text{ mm}$ .

The identified AR were transformed into black and white matrices through a simple "binarization" technique [2] (Figure 4). This technique consists in determining a threshold as a separator between *black* and *white* pixels<sup>2</sup>. The threshold was assigned to the temperature of the brighter regions of each map. If the temperature of a certain pixel was greater than a threshold value, it was assigned the "white pixel" value, while a "black pixel" value was assigned on the contrary. After the "binarization", the Canny Algorithm [12] implemented on the OpenCV library [1] for contour detection was applied. OpenCV is a free library for academic purposes and is divided in several modules, each one addressing a specific problem in computing vision [13].

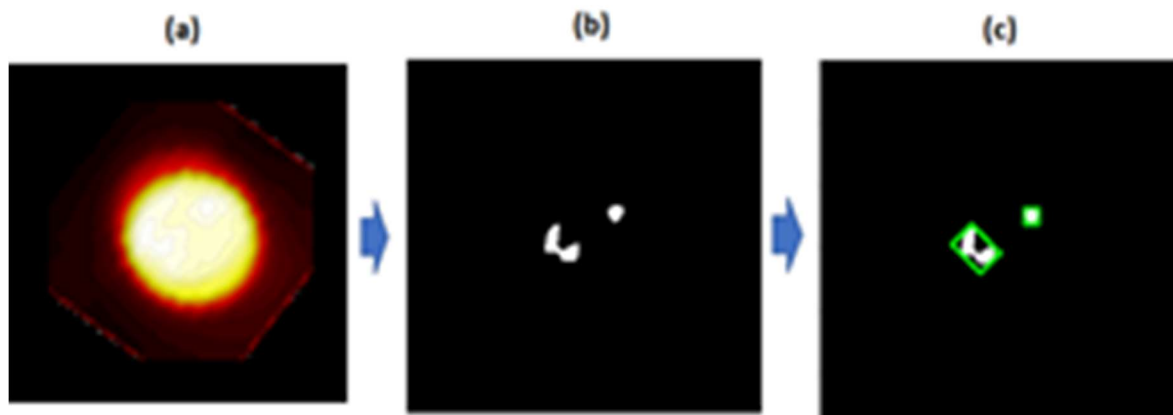


Fig.4: (a) Solar map at 212 GHz, the rectangles mark the AR visually detected; (b) binarization with emphasis on the AR; (c) Contour detection with Canny.

## 4. Results and Discussions

### 4.1 Variation of the Number of AR during the Solar Cycle

To verify the accuracy of the AR detection method, the same algorithm was applied to the 17 GHz NoRH maps. However, we did not need to apply the ConvNet classification: after running our recognition procedure with and without the ConvNet in a subsample we found the same results with both methods. Moreover, an statistical analysis of the

<sup>2</sup> We remember that colors are artificial.

NoRH maps was carried out previously with an automatic AR recognition without the use of any machine learning technique [29].

We obtained a time series with the yearly average number of 17 GHz AR and compared with the sunspot number provided by WDC-SILSO, Royal Observatory of Belgium [30] and SST 212 GHz results. In order to compare with submillimeter results we need to introduce a correction factor since the SST time series is incomplete

$$f = \frac{365}{\text{Number of days with maps in a year}}$$

Results are shown in Figure 5, where we plot the normalized number of 212 GHz AR together with the Sunspot Number and the number of 17 GHz AR. The 17 GHz AR and the Sunspot Number are in excellent agreement as it was observed before [29]. The 212 GHz curve, however, shows marked discrepancies. During the years 2002 – 2007 there is a significant deficit that can be attributed to a low performance of the telescope, a problem that was corrected by late 2006. The deficit in 2014 is due to the small number of observing days, the telescope stopped for months, and the  $f$  factor underestimates the correction. The overall shape of the curve, however, is similar to the sunspot number and the number of 17 GHz AR and we consider as a validation for our procedure.

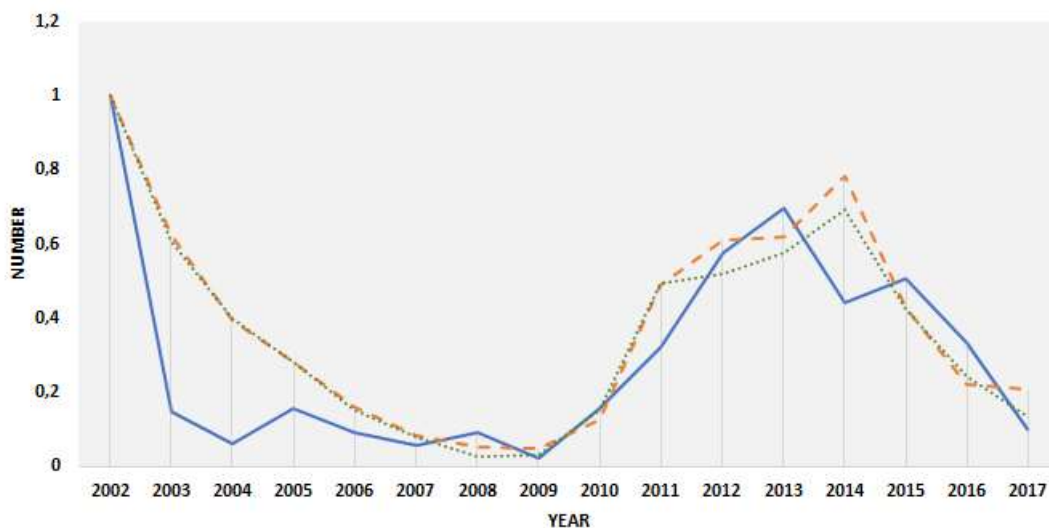


Fig.5: Time evolution of the normalized annual Number of Active Regions at 17 GHz (dashed orange curve), 212 GHz (solid light blue curve) and the Sunspot Index (dotted green curve).

## 4.2 Active Region physical characteristics

Since SST beams are of similar size as the mean AR, we can only derive overall values of their brightness temperatures and sizes. In Figure 6 we show the brightness temperature excess over quiet Sun histograms at 212 and 405 GHz. They are asymmetric at both frequencies, therefore we decided to obtain their mean and the median, that, however, are similar within  $1-\sigma$ : 344 K (5.8% above quiet sun) and 426 K (8.4% above quiet sun) for 212 and 405 GHz respectively. In both cases our values are lower than those reported by Silva et al. [11] who found  $\sim 10\%$  and  $13\%$  increase above the quiet Sun at 212 and 405 GHz respectively; but they are compatible with Loukitcheva et al. [35]

who used ALMA high resolution interferometric images in band 6 (1.3 mm) to make a detailed study of a sunspot. Since 212 GHz beams have a HPBW = 4 arcmin we took the mean  $T_B$  reported by Loukitcheva between the quiet Sun (6000 K), the surrounding plage (7340 K) and the sunspot (6500 K) weighted by the surface yielding  $\sim 6\%$  increase over the quiet sun when observed with the SST at 212 GHz.

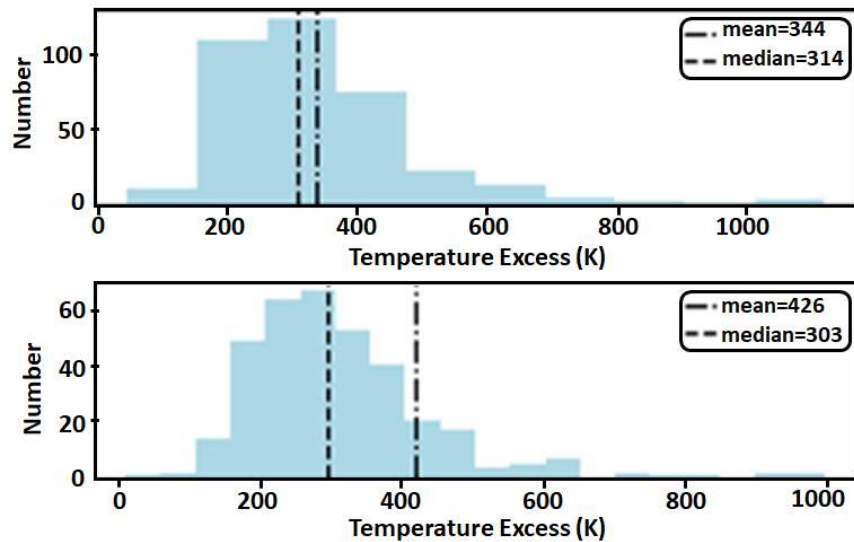


Fig. 6. Histograms of AR brightness temperature excess at 212 (top) and 405 GHz (bottom).

Effective AR sizes are shown in Figure 7, they also have asymmetric distributions, which can be attributed to the lower cut-off represented by the beam sizes. Mean values are  $\phi^{212} = 5$  arcmin and  $\phi^{405} = 4$  arcmin at 212 and 405 GHz respectively. These values are in excellent agreement with [11].

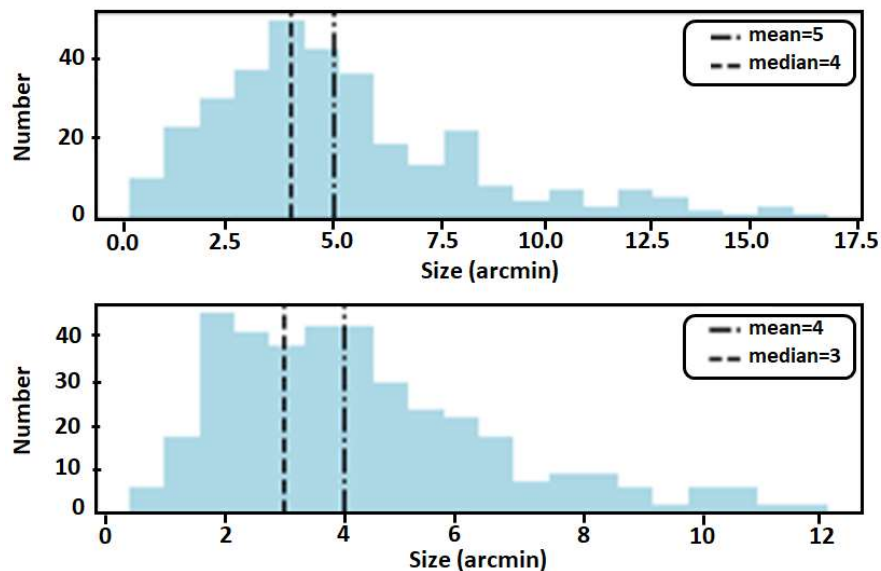


Fig.7. Histograms of the AR effective sizes at 212 (top) and 405 GHz (bottom).

From the brightness temperatures and effective sizes, we can derive the AR flux density for the frequency  $\nu$  of a source with brightness temperature  $T_b$  using the Rayleigh-Jeans black body approximation

$$\mathcal{F}_\nu = \frac{2 k_B T_b \nu^2}{c^2} \Omega ,$$

where  $K_B$  is the Boltzmann constant and  $\Omega$  the effective AR solid angle. Figure 8 presents the obtained flux density histograms for both frequencies, which as the previous ones, are rather asymmetric. The mean values  $F_{212} = 109$  sfu<sup>3</sup> and  $F_{405} = 377$  sfu, are similar to the median values within one standard deviation.

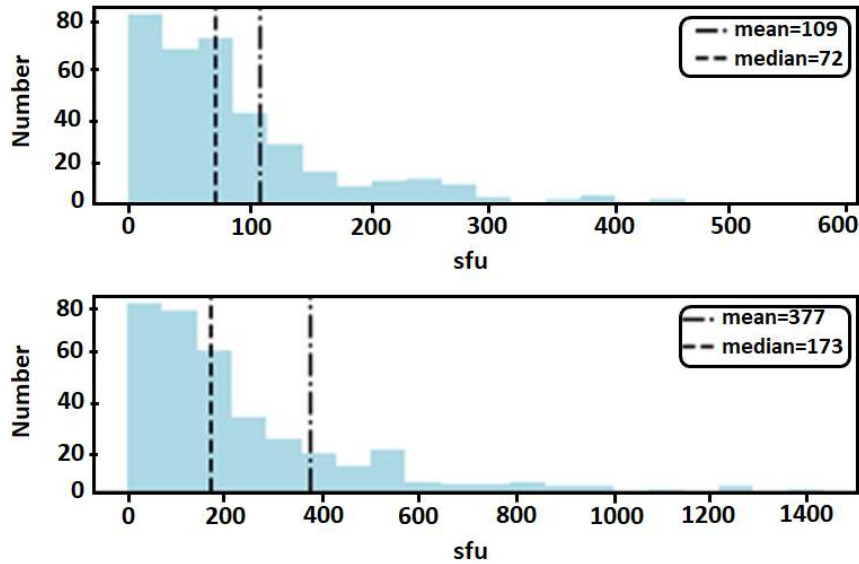


Fig.8. Histograms of the AR flux densities at 212 (top) and 405 GHz (bottom).

We finally derived the spectral index between 405 and 212 GHz for each AR as

$$\alpha = \frac{\log(\mathcal{F}_{405}) - \log(\mathcal{F}_{212})}{\log(405) - \log(212)} ,$$

The histogram (Figure 9) is rather symmetrical, and well represented by a Gaussian distribution with a mean value = 1.58 and  $\sigma = 2.45$ . These values are compatible with an optically thick submillimeter emission and very similar to what was found by Silva et al.

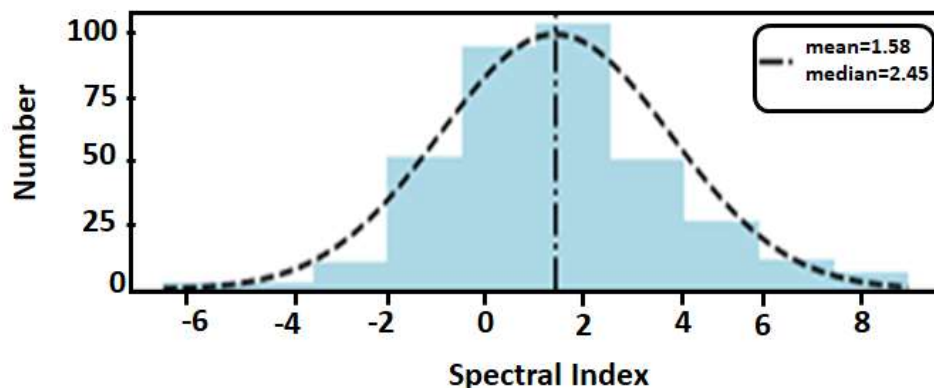


Fig. 9. Histogram of the ARs spectral index between 405 and 212 GHz. The dashed curve is a Gaussian distribution fitting to the data.

<sup>3</sup> Solar Flux Unit (sfu) =  $10^{-22}$  Wm<sup>-2</sup>Hz<sup>-1</sup>

## 5. Conclusions

In this paper, we propose a method for classifying submillimeter solar maps and identify AR, by using a ConvNet, within the Keras framework, and the computing vision API OpenCV. We applied this method to daily solar maps obtained at 212 and 405 GHz with the Solar Submillimeter Telescope, from 2002 and 2017, i.e., encompassing the peak and decaying phase of the solar cycle 23 and almost the whole cycle 24. In the literature, many artificial ConvNet network models are found [14] [15] [16] that can be used to solve a specific problem; in general, the quality of the network architecture improves significantly using deeper and wider networks. Since our main motivation is to demonstrate that the use of convolutional neural networks is useful in assisting in our research, we don't claim that our model is the best or the most efficient.

It has been shown that AR at submillimeter frequencies are weak structures with a maximum intensity  $\leq 10\%$  that of the quiet Sun, and since radiation at high radio frequencies is greatly affected by the atmospheric opacity, it is difficult their identification. Even though, our method was able to automatically identify more than 400 AR. Their statistical characteristics are in good agreement with previous analysis conducted over small samples using visual detection [11], a fact that can be considered as an external verification. Moreover, in spite of the gaps in the submillimeter dataset, the overall variation of the annual number of AR at 212 GHz follows the sunspot number and the number of AR at 17 GHz, which is another external confirmation of the correctness of the proposed method. We note, however, that we found excess brightness temperatures  $T_B$  closer to results obtained with the ALMA interferometer which has a much higher spatial resolution [35] than those with the same instrument in a previous work [11]. What Loukitcheva et al. [35] have found is that the sunspot umbra is cooler while the penumbra is hotter than the surrounding quiet Sun. Since the SST cannot spatially resolve umbra from penumbra, it must inform an effective brightness temperature that includes also a portion of the quiet Sun. Moreover, the statistic used by Silva et al. [11] is based in 23 observing days between May and July 2002 near the solar maximum of cycle 23, that resulted in 16 different AR only. Therefore, it cannot be compared with our  $> 15$  years analysis where two different solar maxima and a solar minimum are included. Actually, we have observed that  $T_B$  varies over the solar cycle, a result that is being published elsewhere; and since Silva et al. [11] data were closer to a solar maximum, while Loukitcheva et al. [35] data correspond to a solar minimum (of a *rather weak* solar cycle) it lends support to our result, which represents a mean value over a long period of time.

The SST is, so far, the only solar patrol telescope at submillimeter frequencies and has beams with sizes smaller than the solar disc, allowing long term studies of quiescent structures on the Sun. The automatic detection of these structures is crucial for statistical analysis that can complement detailed observations with high spatial resolution.

**Acknowledgements.** This work was financed by São Paulo State Funding Agency FAPESP through grant 2013/24155-3 and US Air Force Office for Scientific Research FA9550-16-1-0072. CGGC acknowledges the Brazilian National Funding Agency CNPq the support given through grant 305203/2016-9 and ALGP and JFVS are thankful to Brazilian Postgraduate studies funding agency CAPES. This work is based on data acquired at Complejo Astronómico El Leoncito, operated under agreement between the Consejo

Nacional de Investigaciones Científicas y Técnicas de la República Argentina and the National Universities of La Plata, Córdoba and San Juan.

## References

- [1] “OpenCV”, <https://opencv.org>, 2018.
- [2] González, R. C.; Woods, R. C., *Digital Image Processing*. 3<sup>th</sup> Ed. Pearson Prentice Hall, p. 414-417, 2001.
- [3] Nair, V. and Hinton, G. E., *Rectified linear units improve restricted boltzmann machines*, in Proceedings of the 27th International Conference on Machine Learning (ICML-10), pp. 807–814, 2010.
- [4] O’Shea, K. Nash, R. An Introduction to Convolutional Neural Networks, Cornell University Library, abs/1511.08458, pp. 1-10, Nov, 2015.
- [5] Kaufmann, P. et al. *New telescopes for ground-based solar observations at submillimeter and mid-IR*, SPIE Conference Series, vol. 7012, 2008.
- [6] Hubel, D. H. and Wiesel, T. N., Receptive fields and functional architecture of monkey striate cortex, *The Journal of physiology*, 195(1):215-43, April, 1968.
- [7] “Keras”, <https://keras.io>, 2018.
- [8] F. Chollet, “Keras”, <https://github.com/fchollet/keras>, 2018.
- [9] “TensorFlow”, <https://github.com/tensorflow/tensorflow>, 2018.
- [10] “Theano”, <https://github.com/Theano/Theano>, 2018.
- [11] Silva, A. V.R., Laganá, T.F, Giménez de castro, C.G., Kaufmann, P., Costa, J.E.R., Levato, H & Rovira, M, *Diffuse component spectra of solar active regions at submillimeter wavelengths*, *Solar Physics*, v227, pp265-281, 2005.
- [12] Canny, J. *A computational approach to edge detection*. *IEEE Transactions on Pattern Analysis and Image Understanding*, v18 (6), pp. 679-698, 1986.
- [13] Culjak, I., *A brief introduction to OpenCV*, in Proceedings of the 35th International Convention MIPRO, pp. 1725-1730, 2012
- [14] LeCun. Y. et al. Gradient-based learning applied to document recognition. *Proceedings of the IEEE*, Volume: 86 , Issue: 11 ,pp. 2278-2324, Nov.,1998.
- [15] Krizhevsky, A et al. *Imagenet classification with deep convolutional neural networks*, in *Advances in neural information processing systems*, pp. 1097–1105, 2012.
- [16] Szegedy C. et al. Going deeper with convolutions, *Proceedings of IEEE Conference on Computer Vision and Pattern Recognition (CVPR) 2015*, pp.1-9, Jun. 2015.
- [17] Silva, J.F.V. *Aprimoramento das técnicas observacionais e de calibração do telescópio solar para ondas submilimétricas (SST)*, PhD Thesis, Universidade Prebisteriana Mackenzie, Brazil, 2016.
- [18] Ciresan, D. C. et al. Flexible, High Performance Convolutional Neural Networks for Image Classification, in *Proceedings of the twenty-second International Joint Conference On Artificial Intelligence*, Volume Two, pages: 1237-1242, July, 2011.
- [19] Bishop, C.M., *Pattern Recognition and Machine Learning (Information Science and Statistics)*, Springer-Verlag New York, Inc., Secaucus, NJ, USA, 2006.

- [20] Raschka, S. *Python Machine Learning (Unlock deeper insights into machine learning with this vital guide to cutting-edge predictive analytics)*, Packt Publishing Livery Place, Ltd., Birmingham, B3 2PB, UK, 2015.
- [21] Goodfellow, I. et al. *Deep Learning*. MIT Press, Cambridge, MA. 800 pp. 2016.
- [22] Aloysius, N. and Geetha, M., *A Review on Deep Convolutional Neural Networks*. International Conference on Communication and Signal Processing, IEEE, April 6-8, India, 2017.
- [23] Lemley, J. et al. *Smart Augmentation. Learning an Optimal Data Augmentation Strategy*, IEEE, Vol. 5, pp. 5858–5869. 2017.
- [24] Simonyan, K and Zisserman, A., Very Deep Convolutional Networks for Large-Scale Image Recognition. in *Proceedings of International Conference on Learning Representations (ICLR 2015)*, pp. 1-14, Apr, 2015.
- [25] Menezes, F. and Valio, A., *Solar Radius at Subterahertz Frequencies and its Relation to Solar Activity*, *Solar Physics*, v292, p195, 2017.
- [26] Wang, J., Perez, L.: *The effectiveness of data augmentation in image classification using deep learning*, Technical report no. 300, Stanford University. 2017.
- [27] Li, H et al. *A convolutional neural network cascade for face detection*, in *Proceedings of the IEEE Conference on Computer*, 2015.
- [28] Mrazova, I. and Kukacka, M. *Can Deep Neural Networks Discover Meaningful Pattern Features?* *Procedia Computer Science* v12, pp194–199, 2012
- [29] Selhorst, C.L., Costa, J.E.R., Giménez de Castro, C.G., Valio, A., Pacini, A. A., Shibasaki, K., *The 17 GHz Active Region Number*, *Astrophys. Journal*, 790, 134, 2014.
- [30] SILSO, "<http://www.sidc.be/silso/datafiles>", Royal Observatory of Belgium, Brussels, 2018.
- [31] Van Driel-Gesztelyi, L & Lucie, M., *Evolution of Active Regions*, *Living Reviews in Solar Physics*, v12, doi:10.1007/lrsp-2015-1, 2015.
- [32] Melo, A. M, Kaufmann, P., Giménez de Castro, C.G., Raulin, J.-P., Levato, H., Marún, A., Giuliani, J.L & Pereyra, P., *Submillimeter-wave Atmospheric Transmission at El leoncito, Argentina Andes*, *IEE Transactions on Antennas and Propagation*, vol 53, 4, 1528, 2005.
- [33] Lemen, J.R., Title, A.M., Akin, D.J., Boerner, P.F., Chou, C., Drake, J.F., Duncan, D.W., Edwards, C.G., Friedlaender, F.M., Heyman, G.F., Hurlburt, N.E., Katz, N.L., Kushner, G.D., and, ...: 2012, *The Atmospheric Imaging Assembly (AIA) on the Solar Dynamics Observatory (SDO)*, *Solar Phys.*, 275, 17, 2012.
- [34] Nakajima, H., Nishio, M., Enome, S., Shibasaki, K., et al., *The Nobeyama Radioheliograph*, *IEEE Proceedings*, 82, 705, 1994.
- [35] Loukitcheva, M.A., Iwai, K., Solanki, S.K., White, S.M., and Shimojo, M., *Solar ALMA Observations: Constraining the Chromosphere above Sunspots*, *Astrophys. Jour.*, v850, p35, 2017.

